



Structural Alterations of Hernioplasty Prostheses in Humans: Correlation between X-Ray Micro-Computed Tomography Observations and Histological Investigations

Gabrielle Voisard¹; Andreas Malekos²; Alessandra Patera³; Stephan Carl⁴; Stefan Hartmann²; Michele Griffa⁵; Edoardo Mazza⁶; Dominique Derome⁴; Ze Zhang¹; Gaetan Brochu¹; Robert Guidoin^{1*}

¹Department of Surgery, Faculty of Medicine, Université Laval, and Division of Regenerative Medicine, Centre de Recherche du CHU – Université Laval, Québec, QC, Canada.

²Center for X-ray Analytics, EMPA, Zurich, Switzerland.

³X-Ray Tomography Group, Swiss Light Source, Paul Scherrer Institute, EPFL-PSI, Lausanne, Switzerland.

⁴Laboratory for Multiscale Studies in Building Physics, EMPA, Zurich, Switzerland.

⁵Concrete and Construction Chemistry Laboratory, EMPA, Zurich, Switzerland.

⁶Department of Mechanical and Process Engineering, ETHZ, Zurich, Switzerland.

*Corresponding Author(s): Robert Guidoin

Department of Surgery, Faculty of Medicine, Pavilion Vandry, Université Laval, Québec, QC G1V 0A6, Canada.
Email: robert.guidoin@fmed.ulaval.ca

Abstract

Background: After implantation, prostheses for hernia repair become encapsulated tissue as the result of foreign body reaction possibly causing structural deformations. The aim of this study is to use X-ray microtomography to obtain three-dimensional characterisation of pristine devices to serve as references for explanted prostheses harvested at reoperation and preserved in a solution of formalin. These deformations and tissue interactions were investigated in explants using X-ray micro-computed tomography and histology alike to illustrate their complementary.

Methods: X-ray micro-computed tomography with a laboratory X-ray source was selected to acquire volumetric datasets of pristine devices and explanted hernia prosthetic meshes in voxel sizes between three and seven micrometres. The explants previously fixed in a formalin solution were imaged. The image segmentation of explanted prostheses allows visualisation of their *in-situ* configuration. Qualitative and possibly quantitative three-dimensional information about tissue integration within a foreign structure were obtained without disrupting the architecture. Histological investigations in scanning electron microscopy, light microscopy and transmission electron microscopy helped to explain and show biointegration of hernia prosthetic meshes competing with scar tissue formation.

Received: Oct 18, 2022

Accepted: Nov 03, 2022

Published Online: Nov 07, 2022

Journal: Journal of Abdominal Wall Reconstruction

Publisher: MedDocs Publishers LLC

Online edition: <http://meddocsonline.org/>

Copyright: © Guidoin R (2021). *This Article is distributed under the terms of Creative Commons Attribution 4.0 International License*

Abbreviations: X-ray microtomography (microCT); Prosthesis; Hernia meshes; Hernia repair; Segmentation; 3D structure analysis; Shrinkage.

Cite this article: Voisard G, Malekos A, Patera A, Carl S, Hartmann S, et al. Structural Alterations of Hernioplasty Prostheses in Humans: Correlation Between X-Ray Micro-Computed Tomography Observations and Histological Investigations J Abdom Wall Reconstr. 2022; 5(2): 1010.



Results: The selected pristine devices were successfully imaged in air. Imaging of meshes in water was less conclusive due to the lack of contrast. The explants studied featured local deformations in prosthetic loops. Overlapping loops were more frequent in explanted prostheses compared to controls. Histological analysis demonstrated biointegration of prosthetic structures. Development of the concentric fibrous capsule surrounding each synthetic yarn contributed to the chronic inflammatory response. The encapsulating tissues did not exhibit any sinusoidal structure and led to the formation of fibrosis. The collagen fibres organised themselves to run parallel to the prosthetic surface and were accompanied by foreign body granulomas in the pores between stitches.

Conclusion: Absorption-based X-ray micro-computed tomography was used successfully with both pristine devices and explanted prostheses. MicroCT allowed a better understanding of the sole observation in textile analysis. In vivo deformation in devices occurred locally at loop level as revealed by segmenting and analysing X-ray datasets. The methodology developed is requiring larger samples for better assessment of global deformation. Pathology of explanted devices proved to be complementary to biointegration that evidenced in detail the formation of scar tissue with granulomas bridging the polypropylene stitches.

Introduction

The elegant review of meshes for hernia repair by Wang et al., [1] describes the multiple types of hernias with their risk factors, and the treatment overview. Parietal defects such as hernias in the abdomen or the groin are causing a large spectrum of symptoms such as pressure sensation, pain, lumps, sexual problems, to name of few. They can be corrected with a prosthesis selected in a flow of devices: synthetic or biological composite [2]. From the beginning of modern abdominal surgery introduced by Bassini in 1887 [3] and the popularity gained after Lichteinstein et al.,[4] and Shouldice [5] gave rise to recurrences that have plagued and frustrated generations of surgeons worldwide [6,7]. This important health issue requires surgical repair. Hernia repair is the most common general surgical procedure in industrialised countries [8]. History has shown that surgeons have been creative to come up with effective solutions to repair these defects and to restore proper abdominal wall functions N[9]. The best surgical option remains to be found, but the actual trend is to use prostheses to reinforce this wall defect. The different types of hernias depend on their location and their cause. Abdominal wall reconstruction is a challenging and complex procedure that includes the restoration of the original tissue structure and its previous functions. The abdominal wall comprises distinct layers whose integrity shall be maintained and reinforced. The elastic recovery and the abdominal wall strength shall be guaranteed after reconstruction. The surgical techniques influence considerably the fate of reconstruction at every tissue interface. They will also direct the selection of prostheses: biological, synthetic or composites. The most common synthetic materials currently in use are Polypropylene (PP), Polyester (PE), Polytetrafluorethylene (PTFE), and Polyvinylidene Fluoride (PVDF) [10], while biological ones from diverse sources, such as human and porcine dermis, small intestinal submucosa, are also chosen, mainly in contaminated surgi-

cal fields [11,12]. Although considered as the optimal surgical intervention at the moment, hernia repair with open, laparoscopic or robotic techniques using prosthesis may bring complications [13]. Visualisation of the current device configuration within the tissue could be informative on the source of pain and could provide insights for the future development of prostheses [14]. It is accepted that several types of devices undergo some shrinkage after implantation and a reduction of their physicochemical properties [15]. Prosthetic meshes could expand as well as they shrink [16]. Despite the many designs available, improvements would still be welcome in terms of the biointegration capacity to regenerate fascia function in the body (with similar strength and elasticity), or to allow the tissue ingrowth to rebuild the abdominal wall, while avoiding adverse events such as recurrence, chronic pain (both nociceptive and neuropathic), infection or prosthesis rejection [17].

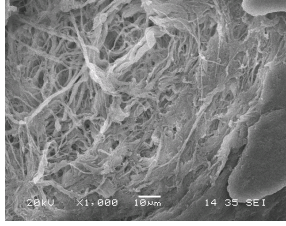
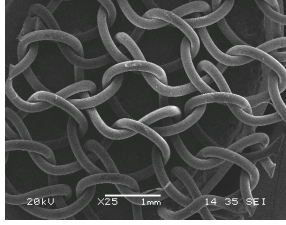
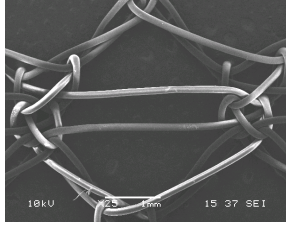
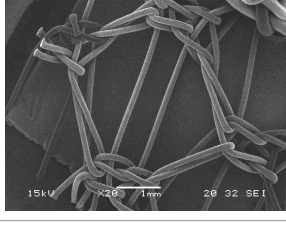
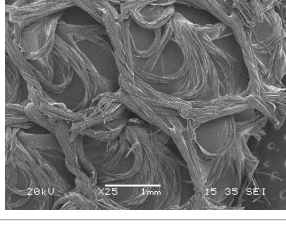
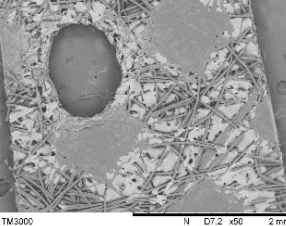
With a view to complement traditional histological features [18] with investigations and physiochemical characterisation, the present work aims at exploring the potential of X-ray micro-computed tomography (XR- μ CT) in three-dimensional documentation for the configuration of pristine devices and explanted prostheses, to a resolution allowing the visualisation of the fibres making them [19,20]. Our hypothesis is that X-ray microCT, known to be a high-resolution non-destructive imaging technique, can offer qualitative and possibly quantitative 3D structural information for the prosthesis without disrupting its architecture after explantation [21]. Similar to CT scanners in hospital, X-ray microtomography scanners use a translate stage to rotate the samples through hundreds of angular views while computing a series of virtual sliced cross-sections [22]. A short object detector and a large source to detector distances guarantee a high spatial resolution. We hereby report developing a specific methodology to acquire and analyse 3D prosthesis datasets, acquiring volumetric data collections on explants for the treatment of inguinal hernia and obtaining qualitative and possibly quantitative 3D information about explanted prostheses compared to controls. Finally, the capacity of this technique to highlight the integration of human tissue through fibres for prostheses using a 3D fashion design is addressed [23,24] in tandem with histopathology [25].

Materials and methods

Selection of prostheses

Five models to serve as controls were selected (Table 1). The AlloMax Surgical Graft is done in human dermis [26]. The Bard Mesh (high weight) and the Bard Soft Mesh (light weight) are polypropylene monofilament warp-knitted fabrics, with respectively small and large pores [27,28]. The Composix L/P Mesh consists of a lightweight monofilament warp-knitted fabric with large pores to face the parietal side and an ePTFE barrier membrane to face the visceral side. The Parietex Composite Mesh is made of polyester monofilament warp-knitted fabrics on the parietal side and a bovine collagen film on the visceral side. The Surgimesh XB is in 100% thermally bonded polypropylene mesh in silicone [29]. Three explanted Bard Mesh prostheses were harvested at surgical explantation and made available for research after pathology observation and fixation in a 10% solution of formaldehyde according to ethical regulations in Canada. Patient-derived explants were by implementing the ethical standards in Switzerland.

Table 1: Selected prostheses.

Name	Manufacturer	Composition	SEM
Allomax Surgical Graft	Bard	Human dermal collagen	
Bard Mesh	Bard	Polypropylene mesh	
Bard Soft Mesh	Bard	Polypropylene mesh	
Composix L/P Mesh	Bard	Large pore polypropylene mesh sewn on expanded PTFE film	
Parietex Composite Mesh	Covidien	Polyester impregnated with a resorbable collagen barrier	
Surgimesh XB	BG Medical	Silicone rubber embedding polypropylene mesh	

Processing of the specimens

From pristine devices, specimens were trimmed in coupons of $5 \times 5 \text{ mm}^2$. Larger samples of Bard Mesh and Bard Soft Mesh were cut as well, but in size of $10 \times 10 \text{ mm}^2$. The explanted Bard Mesh prostheses were prepared in samples of $5 \times 5 \times 5 \text{ mm}^3$ and $10 \times 10 \times 10 \text{ mm}^3$. These were inserted into Kapton tubes (5 mm and 10 mm diameter and 30 mm to 40 mm long) used as specimen holders during beaming time. Control devices were beamed in air and water while the explanted ones were kept in formalin. The specimen holders were vapour tight while being transparent to X-rays.

X-ray microtomography set-up and acquisition

Control coupons and samples of explants were imaged with the X-ray microtomography scanner at the Center for X-ray Analytics at EMPA, in Dübendorf, Switzerland (**Figure 1**). The data acquisition was performed as follows. The element used was an amorphous silicon flat-panel detector (Perkin Elmer 1621-CN3 ES) with 2048×2048 pixels. A thin layer of a CsJ scintillator in front of the detector converts X-ray photons into visible light. Those were then transmitted with a 2D array of amorphous Si-based photodiodes converting finally the visible light into electrical current. No X-ray filter was needed for all samples. Each one was imaged in a 360-degree rotation. The source-to-detector distance remained constant at 1017 mm but the source-to-sample distance varied slightly, and the geometric magnification

for every sample varied accordingly, leading to a voxel size spanning the range from 2.8 μm to 7.07 μm , providing a final spatial resolution for the tomograms was respectively 5 μm to 14 μm . The total acquisition time varied from 24.8 min to 67.5 min, where a single acquisition in raw radiography lasted 68 ms and the number of acquired radiographs per tomogram was either 721 or 1441. The X-ray tube voltage was set within the range of 50 kV to 80 kV and the corresponding electrical current was respectively 200 μA and 100 μA , no hardware binning for the detector was applied. A dark current and a flat plate radiograph were both acquired, for each tomogram, prior to fully imaging the sample, for correction of the outputs by radiography. The tomograms were reconstructed with the Octopus Reconstruction software (Inside Matters). First, sinograms were produced out of the acquired radiographs. Then, a cone beam filtered back-projection algorithm was used for the 3D tomographic reconstruction. The 3D image analysis was performed with the Avizo software (FEI Visualisation Sciences Group) for segmentation and three-dimensional visualisation of the segmented prostheses [30]. The reconstruction from the radiographs led to a tomogram, a three-dimensional image of the object. It consisted of stack-slice manipulations, i.e. axial cross-sections, the plane of these slices being orthogonal to the rotation axis.

Data processing and analysis

The data processing and analysis are detailed in Appendix 1: it includes a full analysis of the segmentation procedure for isolation and visualisation of the prostheses with the Fiji software [31] that implements the algorithm described by Buades [32]. It allows the assessment of the segmented prosthesis integrity and the quantification at loop overlaps [33-35].

Histology

The samples of explanted prostheses and the AlloMax Surgical Graft were divided into three fragments for scanning electron microscopy, light microscopy and transmission electron microscopy [36]. The pristine synthetic devices were only trimmed for scanning electron microscopy without post-fixation of the coupons.

Scanning Electron Microscopy (SEM)

After a post-fixation in a 1% osmium tetroxide solution, the specimens were rinsed in distilled water and dried in ethanol solutions of graded concentrations until absolute ethanol and then transferred in absolute acetone. Final drying was achieved in hexamethyldisilazane. After gold-palladium coating (Sputter Coated Nanotech SEMPRep 2; Nano-Tech Burton-on-Trent, UK), the specimens were observed in scanning electron microscopy at accelerating voltages, from 15 kV to 25 kV (Jeol JSM-6360LV; Tokyo Japan).

Light microscopy

The specimens were cut in narrow strips of 3 mm wide using a microtome at 5 μm thick and embedded in paraffin. Sections were stained with haematoxylin and eosin (HE) for general observations, Masson's trichrome (MT) for collagen and Verhoeff for elastin fibres. The slides were seen in an Axio Imager M2 (Zeiss, Jena, Germany) and the photos were processed with the AxioVision software (Release 4.2.2). For observing the slides in polarised microscopy, they were stained in a Picosirius red solution and rinsed in HCP prior to counter-staining in Harris haematoxylin. The slides were seen using the same microscope, and the photos were done with the AxioVision 9.8_2.0 software [37,38].

Transmission electron microscopy

After a post-fixation in 1% osmium tetroxide solution followed by uranyl acetate staining, the specimens were embedded in epon, and then sliced using an ultra-microtome. Further to additional stains, in lead citrate and uranyl acetate, they were observed in transmission electron microscopy at a voltage of 80 kV (Jeol JEM 1230; Tokyo, Japan) [39,40].

Results

Microtomography

Imaging of the different pristine devices in air resulted in clear 3D reconstructions. The coupons imaged in water offered a loss of information or not at all. The polypropylene was difficult to separate from water because of similar densities. This drawback did not appear with explants, following the incorporation of the mesh into scar tissues.

The overall geometry of explanted prostheses compared to pristine devices was remarkably preserved. However, deformations were present in both. The first ones, more specifically the Bard Soft Mesh, were fitted in the Kapton tube holding the sample and these could not be eliminated based upon the lightness in the structure. As for the second ones, it was the result of tissue encroaching with structural contraction. Therefore, the quantitative analyses showed a great variability ranging from 4.6 mm \pm 1.3 mm to 10.4 mm \pm 2.6 mm in the pristine device and could not be reported in detail.

The three-dimensional visualisation of prostheses illustrating the capacity of microtomography to capture characteristics of each type can be presented as follows. The AlloMax made of human dermis allowed to clearly identify the collagen fibres in air, whereas the structure of the prosthesis in water could not be observed due to similar absorption coefficients. The microstructure of collagen bundles was successfully imaged in air using microCT on this prosthesis, and with pixels of 3.1 μm . The level of detail permitted to analyse its structural density and porosity (**Figure 2: A1 and A2**). A few inaccessible pores were still filled with air and thus were visible in the specimens immersed in water. The wet-dry subtraction from state images could not be performed (**Figure 2: B1 and B2**).

From the Bard Soft Mesh, coupons were carefully cut to fit in the Kapton tube having the same measurements to be imaged in air with coupons of two sizes, 5 \times 5 mm² and 10 \times 10 mm², which resulted in pixels of 3.3 μm and 7.07 μm , respectively, shown in **Figure 3**. A bigger pixel size, i.e. a lower spatial resolution, was enough to capture the geometry of this mesh. The fibre yarn was sufficiently resolved in the whole image. The images acquired were the relaxed geometry of prosthetic mesh because one alveolus had to be kept intact to preserve the architecture. **Figure 4** shows the linear correlation (in red) together with the 3D rendering of a tomogram from CT scanning of Bard Mesh generated in air. The segmentation procedure was further developed to permit a complete 3D visualisation of the mesh (**Figure 5**). The other specimens from pristine devices at 5 \times 5 mm² were based on a propylene fabric imaged in air or water presenting a complex architecture with a sufficient contrast (**Figure 6**).

The tomograms of the composite prostheses are summarised in **Figure 7**. Composit L/P is made of two layers, a polypropylene knitted fabric sewn to a thin expanded PTFE film. The prosthetic knit allows intra-abdominal fixation (parietal side) while the

ePTFE layer (visceral side) prevents adherence. Parietex Composite offers a **specific structure, in a three-dimensional, hexagonal polyester fabric system** (parietal side), applied against a thin collagen sheet (visceral side). The 3D structure observed in this microCT image, confirmed the relevance and interest to acquire such a dataset in three dimensions. Surgimesh featured a bonded polypropylene polymerised into a network impregnated with silicone. To summarise, imaging of the different prostheses in air resulted in clear 3D reconstructions.

The explanted Bard prosthesis as well as the corresponding segmented images are provided in **Figures 8 and 9**. The difference in density between polypropylene yarns and surrounding tissues, then the distinction between the polypropylene yarn and the formalin solution can be reproduced in complex geometries. The $5 \times 5 \times 5 \text{ mm}^3$ explanted specimens demonstrated this reconstruction with a $3\text{--}4 \text{ }\mu\text{m}$ resolution. Excellent results were also obtained with the $10 \times 10 \times 10 \text{ mm}^3$ specimens with a resolution of $7 \text{ }\mu\text{m}$.

The prosthesis was identified through its tissues. The polypropylene yarns were difficult to separate from the formalin solution due to similar densities. The images clearly showed the incorporation of the mesh into the fibrotic capsule surrounding the foreign body of the high and dense implant (**Figure 10**). The overall geometry of the prostheses was well preserved. The qualitative comparison of the two explanted Bard hernia meshes vs. controls illustrated the deformation (**Figure 11**). The average distance between loops displayed a great variation. For each stitch, an average distance between the mesh loop branches and its standard deviation were both computed. The stitches in the meshes as controls revealed a consistent structure where the explanted specimens were deformed and shrank. It was possible to segment one loop from the rest of the prosthesis. The qualitative overlay shows that the scale of the deformation was limited (**Figure 12**).

Histology

The histological analysis of the pristine devices was limited to the AlloMax Surgical Graft and the explanted specimens investigated were the Bard hernia prosthetics. The biological device displayed a skin structure in both light and scanning electron microscopy. In transmission electron microscopy, the collagen bundles were blurry and the bonding of filaments was poorly evidenced because of the delay in the cadaver preservation before skin harvesting and chemical processing. A degradation process began before this process.

The explanted hernia meshes had complete biointegration on the parietal side. The absence of any encapsulation was frequent on the visceral side with dispersed tissues and accumulation of blood debris. Observations in scanning electron microscopy evidenced the parietal aspect of the thick fibrous capsule enmeshing the knitted fabric completely. This capsule was a compact assembly of collagen fibrils. They were parallel to each other and highly stretched under tension without any sinusoidal pattern. The polypropylene yarn began to be weakened with the appearance of thin longitudinal fissures (**Figure 13**).

Light microscopy confirmed the thick encapsulated device. Numerous macrophages featuring foreign body granulomas were surrounding the textile fibres in implantable meshes as the result of the chronic inflammatory response due to surface oxidation and polypropylene shredding. The Masson's trichrome and the Verhoeff's stains allowed visualization of the stretched

collagen fibres. Neither bacteria nor infectious organisms were observed in any of the explanted prostheses. The high level of foreign body granulomas in the voids at the interface of yarns was consequently the outcome of a chronic inflammatory reaction caused by particles shredded that are detached from the oxidised surface of polypropylene (**Figure 14**). The presence of stretched collagen bundles accumulating in parallel layers and surrounded fibres used in prosthetics was notable. The collagen bundles concentrically lay flat around the mesh filaments. They were frequently stretching until rupture, making the wound very stiff. The absence of any waviness in the collagen encapsulation was illustrated in a Picrosirius red staining (**Figure 15**).

The Transmission Electron Microscopy (TEM) added another input to assess the quality of collagen fibres surrounding the explanted prostheses that were elongating under tension until rupture. The filaments themselves are of good quality and parallel to each other. They showed no aggregation with well-individualised filaments. The usual sinusoidal pattern was replaced by stretched longitudinal fibres. This explained why the newly constructed collagen structure that surrounded each yarn of the prostheses was under increasing tension after implantation (**Figure 16**).

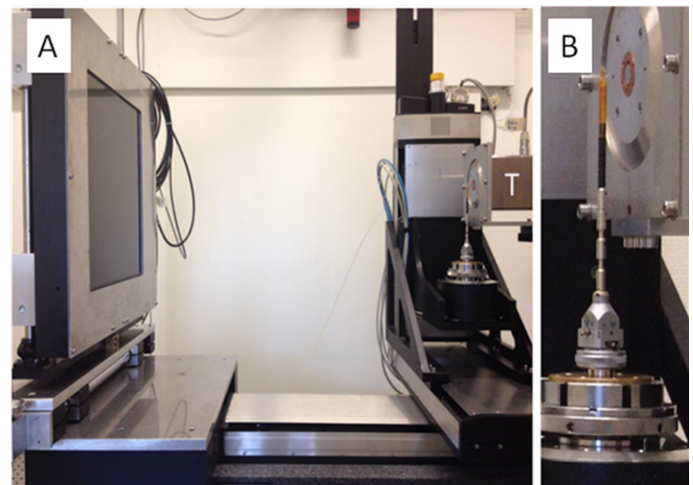


Figure 1: X-ray microtomography set-up with the X-ray tube T (A) and close-up of the Kapton tube holding sample (B).

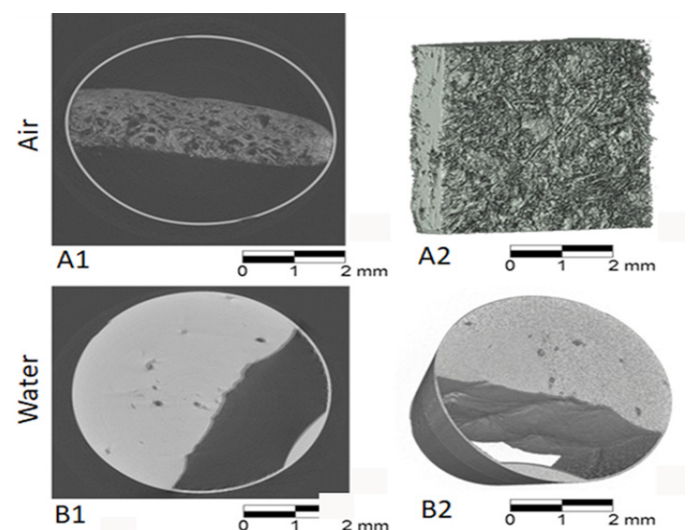


Figure 2: AlloMax hernioplasty prosthesis observed in air and water. Voids are suspected in the cross-section in air (A1), the 3D reconstruction illustrates a fibrous structure without any communicating pores (A2). The water fills the space between the prosthesis and the tube (B1) on one side only (B2).

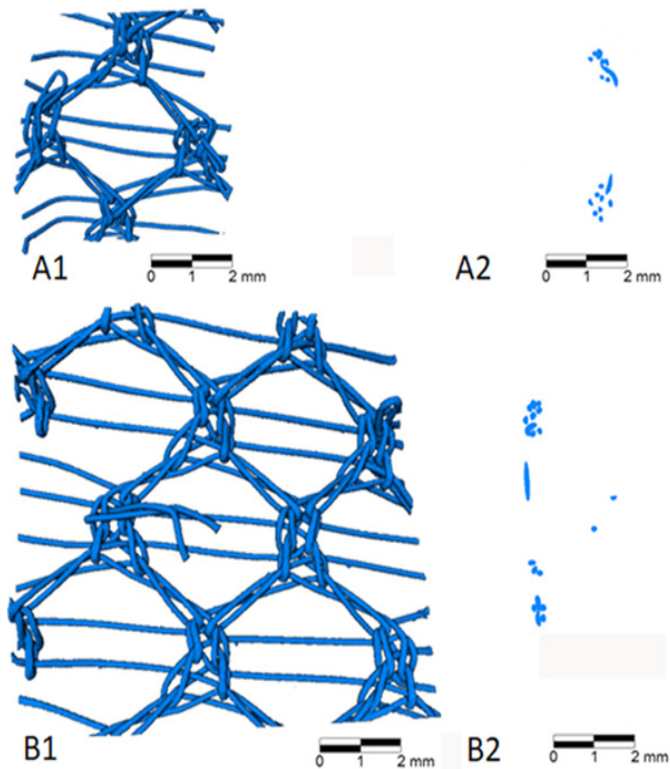


Figure 3: Bard Soft Mesh prosthesis is seen in air. Coupons of two sizes are shown: 5 × 5 mm² (A) vs. 10 × 10 mm² (B): frontal view (A1, B1) and cross-section (A2, B2).

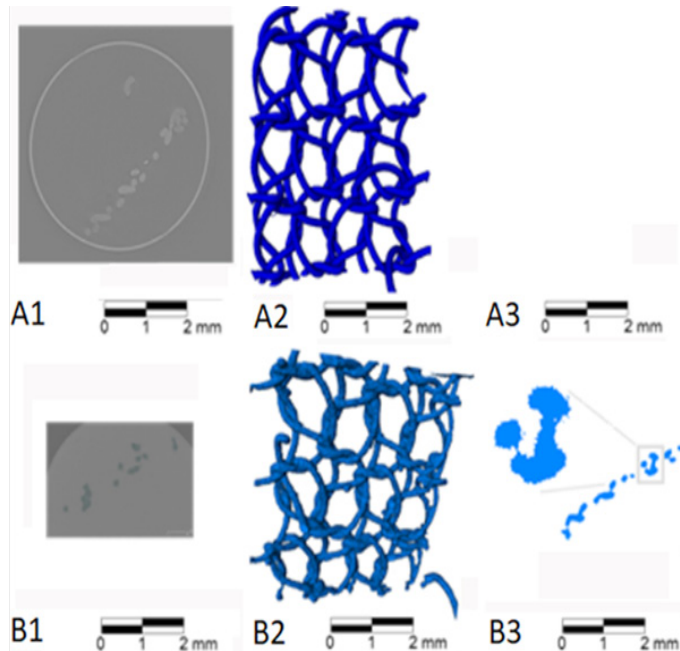


Figure 6: Bard Mesh coupons of 5 × 5 mm² in 3D visualisation in air (A) and water (B): dataset from the tomogram (A1, B1), frontal observations (A2, B2) and cross-sections (A3, B3).

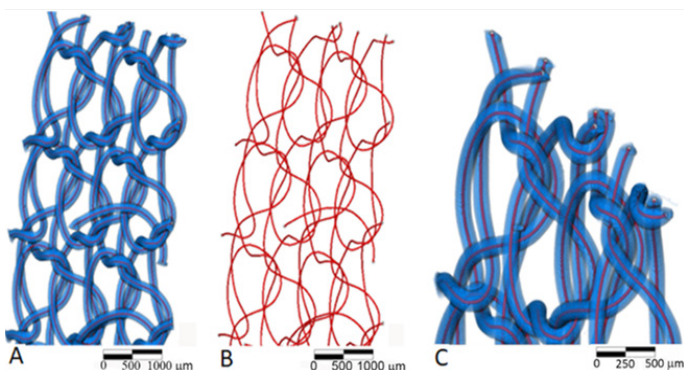


Figure 4: Bard Soft Mesh prosthesis in air. The 3D label image rendering (blue) (A) and corresponding lines (red) (B) illustrate the frontal observation of both mesh and correlation lines. Close-up of isometric frontal observation highlights the overlapping loops of the warp-knitted fabric (C).

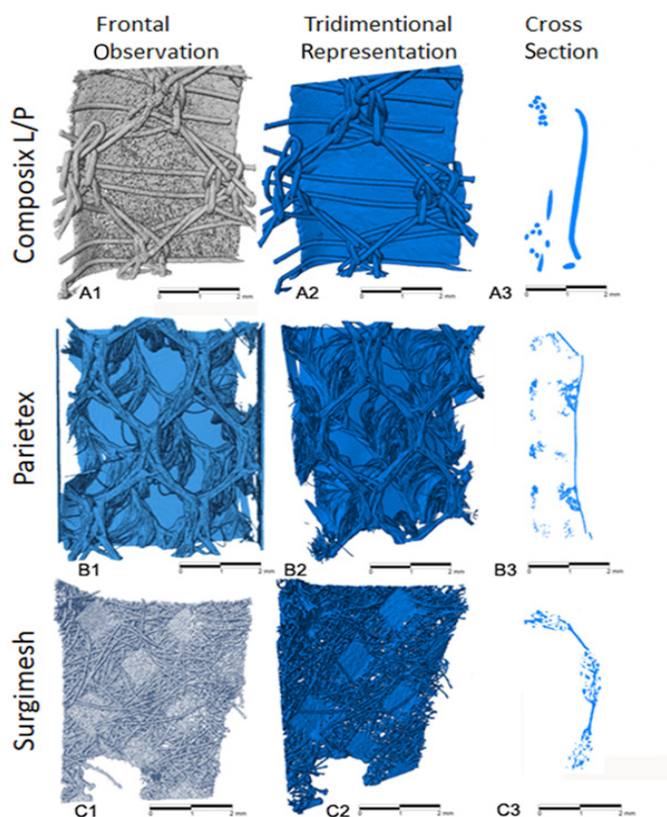


Figure 7: Coupons of composite prostheses: frontal observation, tridimensional representation and cross-section of the Composix L/P made of a lightweight polypropylene warp-knitted construction with an ePTFE barrier on the visceral face (A1, A2, A3), the Parietex in the same polypropylene fabric with an absorbable film of collagen on the visceral face (B1, B2, B3) and the Surgimesh XB whose polypropylene fabric is impregnated with silicone 100% thermally bonded (C1, C2, C3).

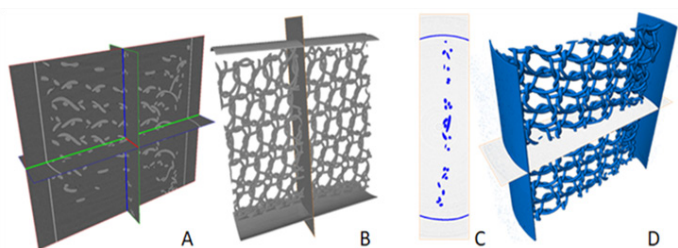


Figure 5: Bard Mesh prosthesis observed in air. The coupon was inserted in a 10 mm diameter tube after segmentation: visualisation of the tomogram using 2D cross-sections orthogonal to each other (A); volume rendering of the raw tomogram (B); cross-section after thresholding (C); volume rendering of the prosthesis segmented by thresholding (D).

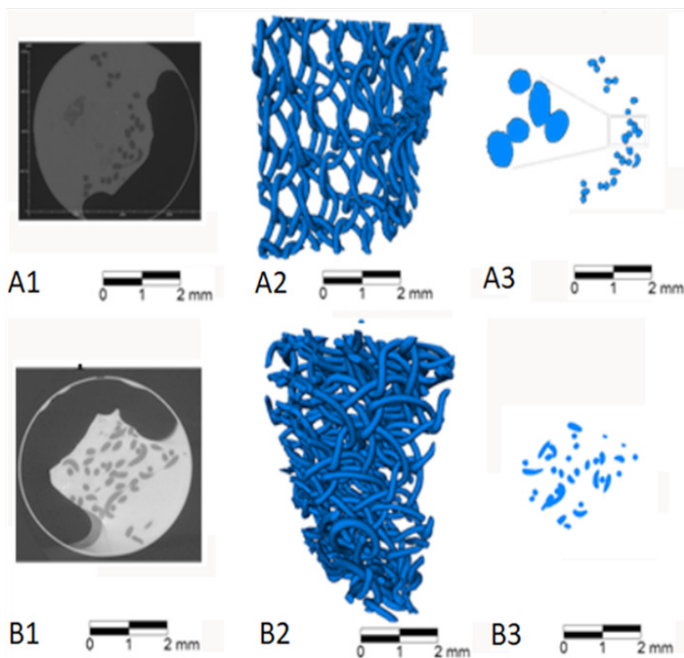


Figure 8: Explanted Bard Mesh prosthesis specimens of $5 \times 5 \times 5 \text{ mm}^3$. Dataset from the tomogram (A1) incorporating a plug (B1), frontal observations (A2, B2) and cross-sections (C1, C2).

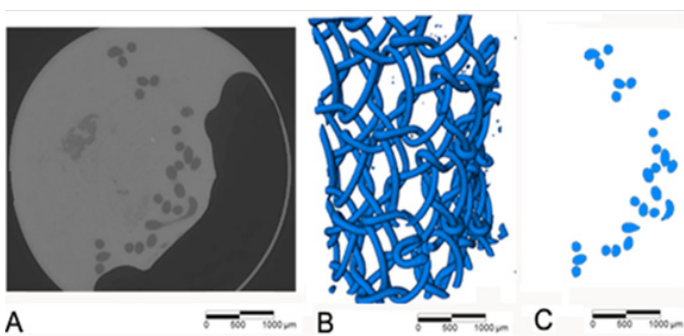


Figure 9: Filtered tomogram of an explanted Bard Mesh prosthesis specimen. The axial cross-section shows tissue encapsulating the fabric structure (A). The frontal view illustrates the irregular shrinking of the fabric (B) and the cross-section shows a regular distribution of the fabric yarns (C).

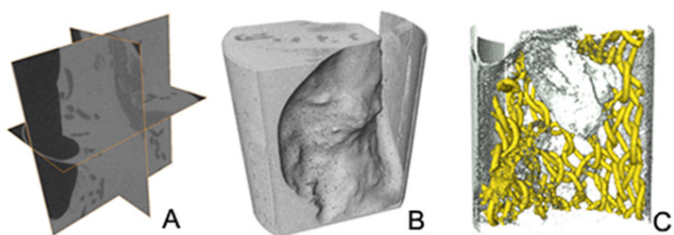


Figure 10: Explanted Bard Mesh prosthesis of $5 \times 5 \times 5 \text{ mm}^3$ observed in a 10 mm diameter tube. The raw tomogram using axial, sagittal and coronal 2D cross-section is illustrated (A), the volume rendering of the tomogram shows the external tissue encapsulation (B), and the multiple color scales confirming the tissue encapsulation of the mesh on the parietal side whereas the visceral side is devoid of any encapsulation with an organised structure (C).

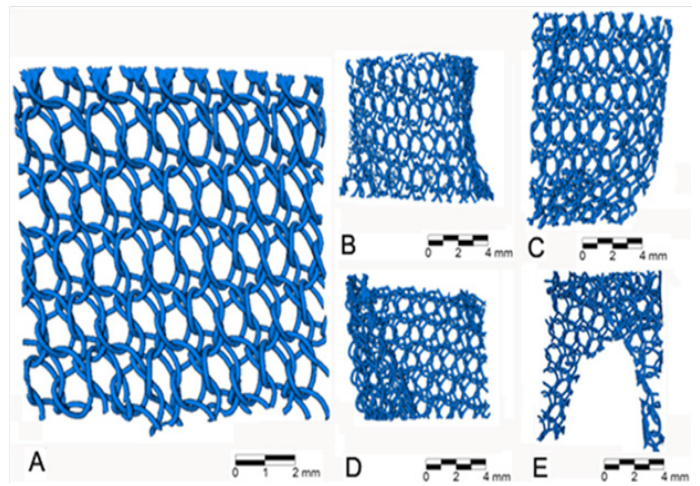


Figure 11: Coupon of a Bard Mesh prosthesis $10 \times 10 \text{ mm}^2$ vs. an explanted specimen $10 \times 10 \times 10 \text{ mm}^3$. The control fabric is flat and the stitches are regularly ordered (A), whereas the explanted specimens are shrunk to different levels (B, C) with eventually some overlapping (D) or restructuring (E).

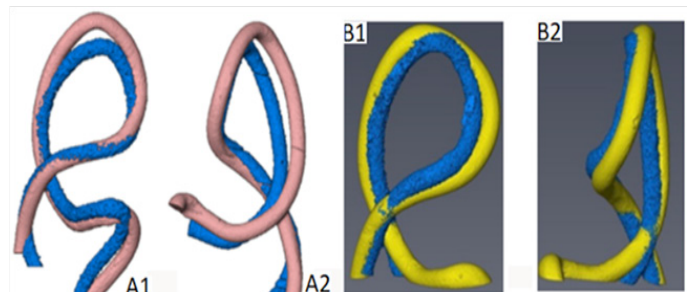


Figure 12: Loops in Bard Mesh prostheses: frontal (A1) and cross-section (A2) of the pristine device, and frontal (B1) and cross-section (B2) of the explanted specimen.

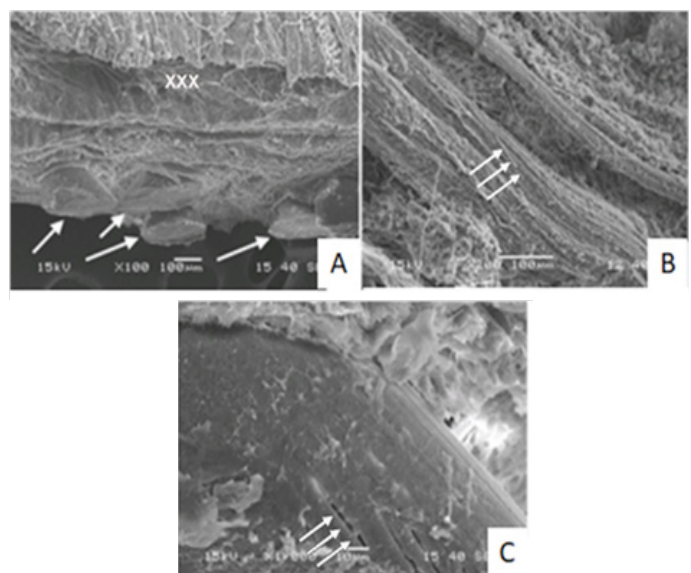


Figure 13: An explanted Bard Mesh specimen in scanning electron microscopy. The external capsule on the parietal side is made of dense fibrous tissues (A, XXX), whereas the polypropylene fabric on the visceral side is devoid of any encapsulation (A, arrows). The connective tissues are well organised on the visceral side with fibrous bundles running parallel to fabric (B, arrows). The polypropylene yarns of the fabric demonstrate some level of fragility as longitudinal fractures are evidenced (C, arrows).

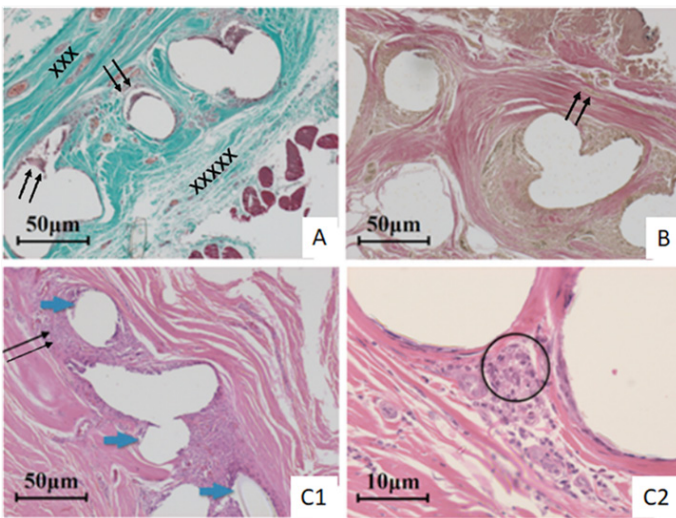


Figure 14: Explanted Bard Mesh prosthesis in light microscopy. The monofilaments encapsulated in yarns of polypropylene show striking differences between the parietal side (A, xxx) and the visceral side (A, xxxxx). Inflammatory cells are accumulating in the vicinity of the polypropylene yarn that reveals early surface degradation (A, arrows) (Masson's trichrome staining). In the absence of severe surface degradation, the encapsulation corresponds to a scar tissue made of elongated fibres of collagen without any sinusoidal patterns, causing the stiffness of the abdominal wall (B, arrows) (Haematoxylin and eosin staining). The surface oxidation of the polypropylene yarn is associated with an encapsulation that shows cracks (C1, blue arrows) and accumulation of macrophages (C1, black arrows), leading to foreign body granulomas in between the yarns (C2, circle) (Haematoxylin and eosin staining).

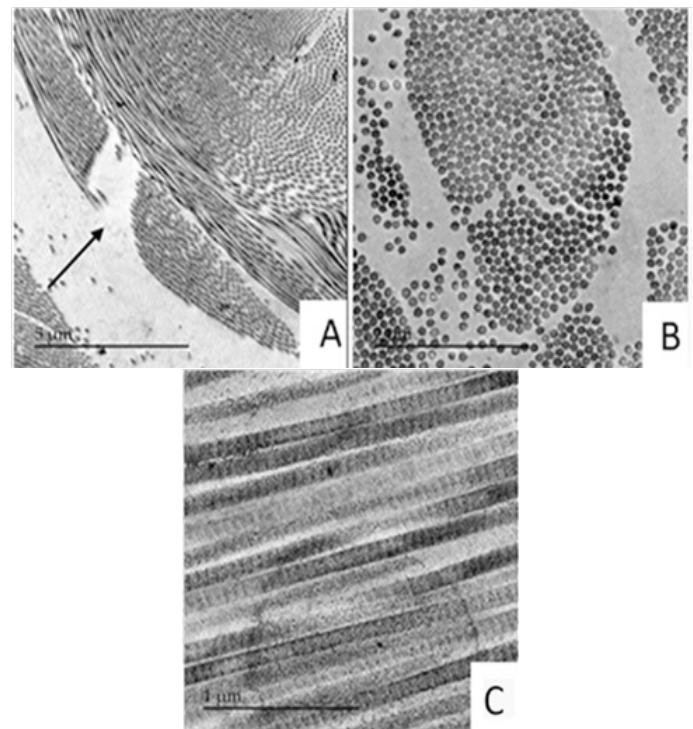


Figure 16: Explanted Bard Mesh prosthesis in transmission electron microscopy. The encapsulation of the polypropylene yarns is made of elongated collagen bundles with various orientations, contributing in the elimination of any elasticity in the scar tissue; such an elongation of the bundles without any sinusoidal patterns can lead to fracture (A, arrow). The fibrils of collagen are individualized, without any agglutination and sign of degradation (B). Those fibrils show a regular banding resulting from the overlap of the tropocollagen constituents (C).

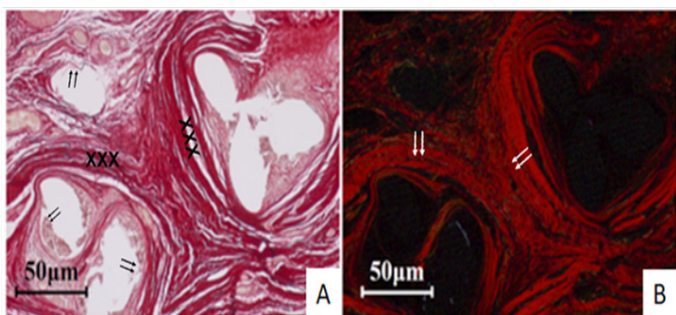


Figure 15: Observation of the polypropylene yarns after Picrosirius red staining in light microscopy (A) and polarised microscopy (B). Inflammatory cells are accumulating in the vicinity of the polypropylene yarns whose oxidised surfaces are cracking (A, arrows) whereas complete encapsulation with individualised elongated collagen fibres of different diameters and embedded the yarn structure (A, xxx). These fibres are predominantly made of type I collagen with well-individualised fibrils in various diameters (B, arrows). The complete absence of sinusoidal patterns explains the lack of elasticity and the stiffness of the scar tissue.

Discussion

More than one million prostheses for a hernia repair are implanted worldwide every year and the modern era started in 1958 with the introduction of polyester and polypropylene fabrics [41,42]. Depending on the technique used, it could be open, laparoscopic or robotic surgery, the prosthesis is in contact with different structures. There is no consensus regarding the most common approach; however, the surgeons are following the guidelines from Hernia Societies [43-45]. The procedure will be considered as successful as the patient stays away from infection, along an absence of short- and long-term recurrence as well as chronic pain. This last point is frequently troublesome

for the patient and end up in medico-legal issues [46-48].

Each prosthesis offers specific characteristics, which make it suitable for different applications in implantology according to the surgeon's practice [49,50]. Any prosthetic device requires one or more components depending on the complexity of its construction and the anticipated function as an implant. The selection of synthetic prostheses for hernia repair is limited to a few polymers, namely polypropylene, polyethylene terephthalate (polyester), Polytetrafluoroethylene (PTFE) and Polyvinylidene Fluoride (PVDF), whereas multiple biological devices from a human or animal sourcing made of tissues chemically processed are available. Most of hernioplasty prostheses currently implanted are therefore made of knitted textiles [51]. The characteristics of the structure, such as inter-yarn distance and density, are important properties taken into consideration when choosing a device to repair an abdominal wall or inguinal defect. Any implant should adhere to the 3 B concept: biofunctionality, biodurability and biocompatibility. The biofunctionality can be defined as the treatment of a deficiency, while the biodurability is related to the stability without deformation and/or degradation whereas the biocompatibility focuses on the biointegration in the absence of an exacerbated chronic inflammatory response and necrosis. The sourcing of synthetic polymers, more specifically the polypropylene cannot rely on a sound traceability since its degradation as reported [52] is frequently challenged. Any prosthesis undergoes different processes once inserted in the body, such as shrinkage, tissue encapsulation being exacerbated or absence of it, adherence formation, structural deformation, and/or chemical degradation of polymers [52]. Most prostheses

are designed as a flat textile, because of knitting patterns. In the meantime, surface treatment or addition of an anti-adhesive coating on the visceral side results in three-dimensional (3D) fabrication, which has been challenging to document, especially when tissues are present [57]. Histological observations in light and electron microscopy are being used to analyse explanted devices. However, these technical approaches necessitate further processing and lead to 2D findings. The information about 3D structure is thus missing. Coda et al. subjected explanted prostheses to a digestion process to eliminate the tissues and found a wide range of alterations, such as shrinkage or swelling of these prosthetic devices. But control prostheses exposed to the same treatment displayed similarities, revealing the sensitivity of materials to this digestion process [16]. Various opposite opinions were then expressed in the literature for fresh tissues [58] and fixed tissues alike [59].

Another competitive strategy to record documentation is Magnetic Resonance Imaging (MRI), for three-dimensional *in vivo* imaging in rats and in case of human hiatal hernia repairs, using MRI visible prostheses [60,61]. Changes in the overall area of the prosthesis before/after the operation could be followed. The microparticles to increase visualisation are also possible, as shown in an image of a pelvic floor mesh at a millimetre resolution [61]. However, in these MRI studies, limitations of spatial resolution do not allow to assess in detail the configuration of the prosthesis and its interaction with surrounding tissues [62].

In medical applications, X-ray micro-computed tomography (XR- μ CT), which can reach micrometre-level resolutions, has mostly been used in relation with orthopaedic, maxillary or vascular surgery, as well as bone, tendon or endovascular prostheses [63-66]. Other types of implants have been imaged, either explanted ones or additional kinds of samples, as three-dimensional data is found highly relevant in many instances, for example in the deployment of a coronary stent [67]. All these applications could go with microCT because of the difference in density, like X-ray attenuation between the various studied materials. To increase this last, a proposed method used special meshes with barium-impregnated borders. However, fabrics of hernia repair prosthesis have fine structure, materials with low X-ray mass attenuation coefficients and so far have not been thoroughly investigated with microCT. Only one study is found using microCT to examine abdominal hernia prosthesis. Sindhvani et al. documented *in vivo* condition of rats, the geometric changes in the prosthesis after implantation at a spatial resolution of 35 μ m per pixel and compared their geometry to the ones in control device samples incorporated into agarose gel [68,69]. The quality of datasets allowed the capturing of dimension changes (up to 16%), those are probably due to either a prosthesis folding or an aggregation of pores during suturing. Further image processing identified decrease in the interpore distance of 4%. A main conclusion of the above-mentioned work is that the process of tissue integration leads to a limited but significant change over time. Finally, the authors state that clinical studies using microCT are not possible because of technological limitations. In fact, standard absorption-based X-ray tomography applied *in situ* on humans cannot achieve sufficient spatial resolution, due to a minimizing radiation dose [70].

MicroCT represents a step forward to better visualise and characterise the implants and thus give directions to improve the physico-chemical characteristics of the prostheses.

The surgeons could benefit from sound information on the constructions and the porosity and density in devices. The manufacturers could provide fine tuning to the most desirable characteristics as the microCT of fabrics has gained great respectability [71-74]. Nevertheless, the analysis of explanted devices is a key issue because it guarantees the evolution for the biofunctionality, corrections of the hernia, biodurability, absence of deformation and/or degradation, biocompatibility and biointegration without any exacerbated inflammation and/or scar tissue growth.

Compared with the results so far reported in the literature and obtained with standards in medical X-ray computed tomography instruments, those outcomes presented in this article carries information to a higher spatial resolution, provided with the micron-size X-ray source which is typical of microCT settings, by comparison with the millimetre one used in the basic imaging methods. The micron-scale light leads to a higher degree of the partial spatially coherent X-ray beam generated, a physical feature which adds up partial X-ray with based on refraction contrast (also called phase contrast in the literature on the radiographs, thus to the final, reconstructed tomograms. For radiographs whose contrast value of every pixel is generated, not only by macroscopic attenuation but by a mix thereof with X-ray refraction, they can provide more information about the location of boundaries between material phases (so-called the "edge enhancement"). As well, they can have higher contrast for low-attenuation materials as with biological tissues [75].

A continuation of such a study requires larger samples for investigations in order to capture the most representative section of the mesh. Also of interest, a method that combines *in vivo* imaging, e.g., a low-dose CT with a microCT procedure for analysing explanted meshes could give full information on complete prostheses. Future research could allow us to estimate *in vivo* configuration and aim at reproducing *in situ* mechanical testing during *ex vivo* microCT.

This study clearly demonstrated the local three-dimensional displacement of the mesh, particularly in loosening the loops which were populated by human tissue. This in itself comprises new information about the method of implanting meshes. Compact collagen, i.e., scar tissue, infiltrates the loops in the prosthesis, as seen in light microscopy [76]. The next needed information would be to identify the type of tissue that is embedding lower density meshes. Whether a low-density structure experiences the same behaviour, or whether the higher distance between yarns would allow for encapsulation with sinusoidal arrangement of collagen fibres to grow in-between them, it is expected by surgeons, patients and manufacturers to preserve the elasticity of the abdominal wall. However, the key issue is to demonstrate the capacity of the microCT to differentiate a polypropylene prosthesis with tissues of lower density [77].

For future clinical studies, a larger sample of explanted prostheses could be imaged to provide a database and allowing the comparison of the current mesh geometry, such as the whole structure folding or shifting, versus its local shrinkage or relaxation. Comparison of 3D information with the clinical background of the patient history, and especially the pain perceived or the symptoms described by him, could contribute to a better identification of the causes. A larger database that includes types of medical observations vs. imaging geometry could lead to establishing a correlation. Ideally, the databank

could be initiated with prosthetic devices from cadavers, adding solid information from asymptomatic implants, thus allowing a comparison between mesh biointegration with and without medical symptoms [78]. The key issue is to determinate the research direction to identify materials and structures capable of curing hernias [79]. The elasticity of tissues shall be addressed as the formation of straight and elongated collagen fibres encapsulating the fabrics, leading to the formation of a scan tissue. The sinusoidal patterns of wavy collagen fibres observed in xenopericardia are necessary to achieve a soft biointegration of the fabrics (**Figure 17**) [80]. The rigidity of any tissue reorganisation and scar formation after damages and diseases shall imperatively be handled, more specifically in case of biomaterial implantation [81]. A plethora of research programs are recommending new avenues to overcome the issue of rigidity, but there will be a long wait after convincing results obtained from the bench are transferred to prosthetic fabrics [82,83]. MicroCT could be the best non-destructive analytical tool to investigate the neo-forming tissues within a polymer structure such as a fabric. However, those results shall be validated in histology.

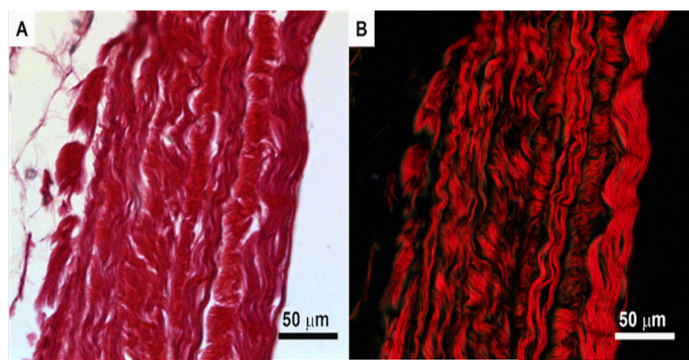


Figure 17: Donkey pericardium after Picosirius red staining in light microscopy (**A**) and polarised microscopy (**B**). Such a construction offers an outstanding degree of elasticity based upon the sinusoidal pattern of the collagen bundles. The development of such a configuration to prevent the rigid encapsulation in any biomaterial is a model to actively pursue to guarantee the long-term success of the prostheses. Such a structure would probably permit the abdominal wall to preserve its elasticity in case of prosthetic hernia meshes.

Conclusion

Volumetric visualisations of synthetic devices, in X-ray microtomography allow structural imaging of pristine devices and explants, with incorporated human tissues. This methodology twinned with detailed histology/scanning electron microscopy, light microscopy and transmission electron microscopy yield results towards a more extensive understanding of the interaction in vivo with a foreign prosthesis, and therefore explaining the reasons for their explantation.

Acknowledgements

Part of this work has been performed by the use of the EMPA Platform for Image Analysis, <http://empa.ch/web/s499/software/-imaging-platform>, at the EMPA Center for X-ray Analytics. We thank Peter Westenberger for support in image analysis. We are indebted to Lucie Germain and Eric Philippe for help and guidance. We thank Véronique Gagné and Dominique Fournier for respectively having typed and proofed the manuscript.

Author's Contributions

G.B., R.G. and D.D. conceived and directed the research; G.V.,

G.B., R.G. and D.D. determined the experimental methodology; E.M., M.G. and A.P. provided guidance in the analysis procedure; G.V., S.C. and S.H. performed X-ray CT acquisition; G.V. and A.M. performed image analysis; R.G. and Z.Z. performed the histology, TEM, SEM imaging; G.V., G.B., R.G., E.M. D.D. and Z.Z. analysed the results. All authors contributed to the scientific discussions and the preparation and writing of the manuscript.

Declaration of conflict of interest:

Authors declares no conflict of interest.

References

1. Wang SC, Kim T, Zhu D. Hernia mesh and hernia repair: a review. *Eng Regen*. 2020; 19-33: 2666-1381.
2. Rodriguez M, Gómez-Gil V, Pérez-Kölher B, Pascual G, Bellán JM. Polymer hernia repair materials: adapting to patient needs and surgical techniques. *Materials* 2021; 14: 2790.
3. Bassini E. About the treatment of the break in the cable. *Archive for Clinical Surgery (Berlin)*. 1890; 40: 429-476.
4. Lichteinstein IL, Shulman AG, AMid PK, Montlov MM. The tension-free hernioplasty. *Am J Surg*. 1989; 157: 188-193.
5. Shouldice EB. The Shouldice repair for groin hernias. *Surg Clin North Am*. 2003; 83: 1163-1187.
6. DeBord JR. The historical development of prosthetics in hernia surgery. *Surg Clin North Am*. 1998; 78: 973-1006.
7. Mokete M, Earnshaw JJ. Evolution of an inguinal hernia surgery practice. *Postgrad Med J*. 2001; 77: 188-190.
8. Berger D. Evidence-based hernia treatment in adults. *Deutsches Aerztebl Int*. 2016; 113: 150-157.
9. Read RC. Milestones in the history of hernia surgery: prosthetic repair. *Hernia*. 2004; 8: 8-14.
10. Zhu LM, Shuster P, Klinge U. Mesh implants: an overview of crucial mesh parameters. *World J Gastrointest Surg*. 2015; 7: 226-236.
11. Smart NJ, Marshall M, Daniels IR. Biological meshes: a review of their use in abdominal wall hernia repairs. *Surgeon*. 2012 ; 10: 159-171.
12. Slater NJ, van der Kolk M, Hendriks T, van Goor H, Bleichrodt RP. Biologic grafts for ventral hernia repair: a systematic review. *Am J Surg*. 2013; 205: 220-230.
13. Burton V, Perez AJ. Comparison of open and laparoscopic inguinal hernia repair. *Mini-invasive Surg*. 2021; 5: 26.
14. Bendavid R, Lou W, Grischkan D, Koch A, Petersen K, et al. A mechanism of mesh-related post herniorrhaphy neuralgia. *Hernia*. 2016; 20: 357-365.
15. Ozog Y, Konstantinovic ML, Werbrouck E, De Ridder D, Mazza E, et al. Shrinkage and biomechanical evaluation of lightweight synthetics in a rabbit model for primary fascial repair. *Int Urogynecol J*. 2011; 22: 1099-1108.
16. Coda A, Bendavid R, Botto-Micca F, Bossotti M, Bona A. Structural alterations of prosthetic meshes in humans. *Hernia*. 2003; 7: 29-34.
17. Salgaonkar H, Lomanto D. Mesh technology. An update. *Ann Laparosc Endosc Surg*. 2018; 3: 82.
18. Cotton B. Quantitative histological analysis of fixation points on explanted hernia mesh. *MSC Dissertation. Clemson University USA*, 2018. All theses 2953.

19. Fisher R, Schlepütz CM, Rossi RM, Derome D, Carmeliet J. Wicking through complex interfaces at interlying yarns. *J Coll Interf Sci.* 2022; 626: 416-425.
20. Desplentere F, Lomov SV, Woerdeman DL, Verpoest I, Wevers M, et al. Micro-CT characterization of variability in 3D textile architecture. *Comput Sci Technol.* 2005; 65: 1920-1930.
21. Garcea SC, Wang Y, Withers PJ. X-ray computed tomography of polymer composites. *Comput Sci Technol.* 2018; 156: 305-319.
22. Elliott JC, Dover SD. X-ray microtomography. *J. Microsc.* 1982; 126: 211-213.
23. Galdberg RE, Duvall CL, Peister A, Oest ME, Lin ASP, et al. 3D imaging of tissue integration with porous biomaterials. *Biomaterials* 2008; 29: 3757-3761.
24. Cengiz IF, Oliveira JM, Reis RL. Micro-CT a digital 3D microstructural voyage into scaffolds: a systematic review of the reported methods and results. *Biomater. Res.* 2018; 22: 26.
25. Rousselle SD, Ramot Y, Nyska A, Jackson ND. Pathology of bioabsorbable implants in preclinical studies. *Toxicol Pathol.* 2019; 47: 358-378.
26. Reznichenko AA. Different biologic grafts for diaphragmatic crura reinforcement during laparoscopic repair of large trial hernia: a six year single surgeon experience. *J Curr Surg.* 2016; 6: 6-13.
27. Sajid MS, Leaver C, Baig MK, Sains P. Systematic review and meta-analysis of the use of lightweight versus heavyweight mesh in open inguinal hernia repair. *Br J Surg.* 2012; 99: 29-37.
28. Miao L, Wang F, Wang L, Zou T, Brochu G, et al. Physical characteristics of medical textile prostheses designed for hernia repair: a comprehensive analysis of select commercial devices. *Materials* 2015; 8: 8148-8168.
29. Serrano-Aroca A, Pons-Serrano A. Prosthetic meshes for hernia repair: state of art, classification, biomaterials, antimicrobial approaches and fabrication methods. *J Biomed Mater Res.* 2021; 109: 2695-2719.
30. Lore C. USG announces the release of Aviso Fire 7, 3D visualization and analysis of software for industrial inspection and materials research. 2018.
31. Schindelin J, Arganda-Carreras I, Frise K, Kayrig V, Longair M, et al. Fiji: an open-source platform for biological-image analysis. *Nat Methods.* 2012; 9: 672-682.
32. Buades A, Coll B, Morel JM. A non-local algorithm for image denoising. *IEEE Computer Society Conference on Computer Vision and Pattern Recognition (CUPR'05). Proceed. IEEE Conf. San-Diego USA.* 2005; 60-65.
33. Roseman AM. Particle finding in electron micrographs using a first local correlation algorithm. *Ultramicroscopy.* 2003; 94: 225-236.
34. Weber B, Greenar G, Prohuska S, Braun D, Hege HC, et al. Automated tracing of microbules in electron tomograms of plastic embedded samples of *Caenorhabditis elegans* embryos. *J. Struct. Biol.* 2012; 178: 129-138.
35. Canny J. A computational approach to edge detection *IEEE Transactions on Patters Analysis and Machine Intelligence. PAMI.* 1986; 8: 679-698.
36. Mao J, Rassoli A, Tony Y, Ronse EN, Le-Bel G, et al. Donkey pericardium compares favorably with commercial xenopericardia used in the manufacture of transcatheter heart in the manufacture of transcatheter heart valves. *Artif Organs.* 2019; 43: 976-987.
37. Zhang H, Sun L, Wang W, Ma X. Quantitative analysis of fibrosis formation on the microcapsule surface with the use of picrosirius red staining, polarized light microscopy and digital image analysis. *J Biomed Mater Res A.* 2006; 76: 120-125.
38. Lattouf R, Yourres R, Lutomski D, Naaman N, Godeau G, et al. Picrosirius red staining: a useful tool to appraise collagen networks in normal and pathological tissues. *J Histochem Cytochem.* 2014; 62: 751-758.
39. Ushiki T. Collagen fibers, reticular fibers and elastic fibers. A comprehensive understanding from a morphological viewpoint. *Ann Histol Cytol.* 2002; 65: 109-126.
40. Kadler KE, Holmer DF, Trottier JA, Chapman JA. Collagen fibril formation. *Biochem J.* 1996; 316: 1-11.
41. Poussier M, Denève E, Blanc P, Boulay E, Bertrand M, et al. A review of available prosthetic maternal for abdominal wall repair. *J Viscer Surg.* 2013; 150: 52-59.
42. Brown CN, Finch JG. Which mesh for hernia repair? *Ann Roy Coll Surg Engl.* 2010; 92: 272-278.
43. Simons MB, Aufenacker T, Bay-Nielson M, Bouillot JL, Campanelli G, et al. European Hernia Society Guidelines on the treatment of inguinal hernia in adult patients. *Hernia.* 2009; 13: 343-403.
44. Muysom FE, Antoniou SA, Bury K, Campanelli G, Conze J, et al. European Hernia Society guidelines on the closure of abdominal wall incisions. *Hernia.* 2015; 19: 1-24.
45. Henriksen NA, Montgomery A, Kaufmann R, Berrevoet F, East B, et al. Guidelines for treatment of umbilical and epigastric hernias from the European Hernia Society and American Hernia Society. *Br. J. Surg.* 2020; 107: 171-190.
46. Varley R, Lo C, Alkhaffaf B. Litigations claims following laparoscopic and open inguinal hernia repairs. *Hernia.* 2020; 24: 1113-1120.
47. Levin, Papantonio, Rafferty. Hernia mesh lawsuit. Injuries, settlements and compensation. 2020.
48. Smith MJ. Hernia mesh and litigation: where things stand. *General Surgery News.* 2022.
49. Bachman S, Ramshaw B. Prosthetic material in ventral hernia repair: how do I chose? *Surg Clin North Am.* 2008; 88: 101-112.
50. Tandafir AF, Popa DE, Vasile D. Prostheses used in laparoscopic inguinal hernia repair: biocompatibility, post-operative complications and quality of life. Review of the literature. *Medica J Clin Med.* 2017; 12: 202-207.
51. Kalaba S, Gerhard E, Winder JS, Pauli EM, Haluck RS, et al. Design strategies and applications of materials and devices for hernia repair. *Bioact Mater.* 2016; 1: 2-17.
52. Iakolev VV, Guelcher SA, Bendavid R. Degradation of polypropylene in vivo: a microscopic analysis of meshes explanted from patients. *J Biomed Mater. Res B Appl Biomater.* 2017; 105: 237-247.
53. McDermott MK, Isayeva IS, Thomas TM, Lee AS, Lucas AD, et al. Characterization of the structure and properties of authentic and counterfeit polypropylene surgical meshes. *Hernia.* 2006; 10: 131-142.
54. Thames SF, White JB, Ong KL. The myth: in vivo degradation of polypropylene-based meshes. *Int Urogynecol J.* 2017; 28: 285-297.
55. Thames SF, White JB, Ong KL. Reply to: In vivo polypropylene mesh degradation in hardly a myth. *Int Urogynecol J.* 2017; 28: 337-338.

56. Fowler DL. How a surgeon can be certain? *Hernia*. 2006; 10: 108-109.
57. Zhu LM, Schuster P, Klinge V. Mesh implants: an overview of crucial mesh parameters. *World J Gastroint Surg*. 2015; 7: 226-236.
58. Zhang Z, Guidoin R, King MW, How TV, Marois Y, et al. Removing fresh tissue from explanted polyurethane prostheses: which approach facilitates physico-chemical analysis? *Biomaterials*. 1995; 16: 369-380.
59. Needham DK, Buchanan DR, Gupta BS, Horton HR. Enzymatic removal of formalin-fixed tissues from polyester arteries and its effects on physical properties of fibers. *J Biomed Mater Res*. 1982; 16: 659-668.
60. Kuehnert N, Kraemer NA, Otto J, Donker HC, Slabu I, et al. In vivo MRI visualization of mesh shrinkage using surgical implants loaded with superparamagnetic iron oxides. *Surg Endosc*. 2012; 26: 1468-1475.
61. Köhler G, Pallwein-Prettner L, Lechner M, Spaun GO, Koch OO, et al. First human magnetic resonance visualisation of prosthetics for laparoscopic large hiatal hernia repair. *Hernia*. 2015; 19: 975-982.
62. Sindhvani N, Feolo A, De Keyzer F, Claus F, Callewaert G, et al. Three-dimensional analysis of implanted magnetic-resonance-visible meshes. *Int Urogynecol J*. 2015; 26: 1459-1465.
63. Papozoglou AS, Karagiannidis E, Maysidis DV, Sofidis G, Bompoti A, et al. Current clinical applications and potential perspective of micro-computed tomography in cardiovascular imaging. A systematic scoping review. *Hellen J Cardiol*. 2021; 62: 399-407.
64. Foerst J, Ball T, Kaplan AV. Post-mortem in situ microCT evaluation of coronary stent fracture. *Catheter Cardiovasc. Interv*. 2010; 76: 527-531.
65. Campioni I, Pecci R, Bedini R. Ten years of microCT in dentistry and maxilla-facial surgery: a literature overview. *Appl Sci*. 2020; 10: 4328.
66. Longo AB, Salmon PL, Ward WC. Comparison of ex-vivo and in vivo micro-computed tomography of rabbit tibia at different scanning. *Settings J Orthop Res*. 2017; 35:1690-1698.
67. Connolley T, Nash D, Baffiere JY, Sharif F, McHugh PE. X-ray micro-tomography of a coronary stent deployed in a model artery. *Med Eng Phys*. 2007; 29: 1132-1141.
68. Sindhvani N, Liaquat Z, Urbankova I, Van de Velde G, Feola A, et al. Immediate postoperative changes in synthetic meshes -in vivo measurements. *J Mech Behav Biomed Mater*. 2015; 55: 228-235.
69. Palma P, Riccetto C, Fraga R, Miyaoka R, Prando A. Dynamic evaluation of pelvic floor reconstructive surgery using radiopaque meshes and three-dimensional helical CT. *Int Braz J Urol*. 2010; 36: 209-217.
70. Bravin A, Coan P, and Suortti P. X-ray phase-contrast imaging: from pre-clinical applications towards clinics. *Phys Med Biol*. 2013; 58: R1-R35.
71. Baby R. Micro and macro-scale analysis of frictional interaction between human skin and woven fabrics. PhD Dissertation, NCSU, Raleigh USA 2021.
72. Baby R, Michielsen S, Wu J. Effects of yarn size and blood drop size on wicking and blood stains in textile. *J Forensic Sci*. 2021; 66: 1246-1256.
73. Wu J, Michielsen S, Baby R. Impact spatter blood stain patterns on textiles. *J Forensic Sci*. 2019; 64: 702-720.
74. Baby R, Mathew K, DenHartog E. Non destructive quantitative evaluation of yarns and fabrics and determination of contact area fabrics using the X-ray microcomputed tomography system for skin-textile friction analysis. *ACS Appl Mater Interfaces*. 2021; 13: 4652-4664.
75. Lee JH, Lee YJ, Cho HJ, Shin H. Guidance of in vitro migration of human mesenchymal stem cells and in vivo guided bone regeneration using aligned electrospun fibers. *Tissue Eng Part A*. 2014; 20: 2031-2042.
76. Gigante A, Busilacchi A, Lonzi B, Cecconi S, Manzotti S, et al. Purified collagen I oriented membrane for tendon repair: an ex vivo morphological study. *J Orthop Res*. 2014; 31: 738-745.
77. Farr NTH, Roman S, Schäfer J, Quade A, Lester D, et al. A novel characterization approach to reveal the mechano-chemical effects to oxidation and dynamic distension of polypropylene surgical mesh. *RSC Adv*. 2021; 11: 34710.
78. Petersen K, Morrison J, Oprea V, Grischkan D, Koch A, et al. Necessary duration of follow-up to assess complications of mesh in hernia surgery: a time-lapse study based on 460 explants. *Hernia*. 2021; 25: 1239-1251.
79. Wang H, Klosterhalfen B, Müllen A, Otto T, Dievernich A, et al. Degradation resistance of PVDF mesh in vivo in comparison to PP mesh. *J Mechr Behav Biomed Med*. 2021; 119: 104490.
80. RAssoli A, Li Y, Bao X, Kawecki F, Zhao X, et al. Donkey pericardium as a select sourcing to manufacture percutaneous heart valves: decellularization has not yet demonstrated any clear cut advantage to glutaraldehyde treatment. *Med Novel Technol Dev*. 2019; 4: 100029.
81. Park JM, Jo SB, Lee JH, Lee HH, Knowles JC, et al. Materials and extracellular matrix rigidity highlighted in tissue damages and diseases: implications for biomaterials design and therapeutic targets. *Bioact Mater*. 2023; 20: 381-403.
82. Kristen M, Ainsworth MJ, Chirico N, van der Ven CFT, Doevendans PA, et al. Fiber scaffold patterning for mending hearts: 3D organization bringing the next step. *Adv Healthcare Mat*. 2020; 9: 1900775.
83. Zieliński PS, Gudeti PKR, Rikmanspoel T, Włodarczyk-Biegun MK. 3D printing of bio-instructive materials: toward directing the cell. *Bioact Mater*. 2023; 19: 292-327.

Appendix 1

Data processing and analysis

A1. Segmentation procedure for isolation and visualisation of the prostheses

Each tomogram was initially subjected to an edge-preserving noise reduction filtering performed with the Fiji software (A1) using the “Non-Local Denoising” plugin. It implements the algorithm to increase the signal-to-noise ratio of the tomograms without significant modifications of the interfaces between different regions belonging to distinct material phases, e.g., between air and tissue, between tissue regions with different mass density or of distinct histological types (A2). The latter feature was the edge preservation property of the algorithm, not only straight interfaces but also those that are very curvy. Once filtered, the tomogram was segmented, i.e., its voxels were divided into two classes corresponding to distinct material phases. The voxels belonging to the prosthesis were assigned a value of one while all the other ones a value of zero. The segmentation was performed with the Avizo 3D software using a simple manual threshold selection, with the voxels having values above the threshold being classified as prosthesis ones (A3).

The process to segment the mesh geometry from the background was straightforward for the pristine prosthesis imaged in air. The contrast between the background (air) and the foreground (mesh) was sufficient to allow the segmentation using thresholding, without the use of a filter. The threshold was selected manually based on a clear partitioning of the voxel value histogram into two distinct Gaussian-like distributions with little overlapping between them. The minimum point between the two peaks of the two distributions was identified as the threshold voxel value. The histogram voxel values in the tomograms for explanted prostheses consisted of three Gaussian-like curves slightly overlapping each other, with as many corresponding and well-resolved peaks. The valleys separating two peaks allowed the definition of threshold voxel values for a clear classification of voxels belonging to air, tissue and mesh, respectively. A good separation of the mesh from surrounding background air and tissue was achieved. The relative homogeneity of the materials, compared to the tissues helped identify the boundary between the different parts, at the scale of the tomogram spatial resolution. The selection of voxel values was done iteratively in order to segment the object volume from the surroundings.

A2. Details of analysis procedures

A21. Assessment of the mesh integrity in segmented prosthesis

The skeleton of the textile was visualised to verify that the mesh was complete and not over-segmented. The centre line of each yarn was traced using the “Cylinder Correlation” and “Trace Correlation Lines” modules in Avizo 3D. The “Cylinder Correlation” module was first applied to the segmented tomogram. This computed normalised cross-correlation of an image with a cylinder. The approach theory was described by Roseman (A4) and this module implements specifically the algorithm outlined by Weber (A5). Two new datasets were produced: a correlation field that stored the maximum cross correlating and the orientation field in which the cylinder at each point is oriented. The correlation field was a tomogram itself, i.e., a 3D image, where larger voxel values corresponded to a better fit. This information was used by the “Trace Correlation Lines” module to trace the centre lines (A6).

A22. Quantification of displacement at loop overlaps

The distance at overlap of loops in the mesh was selected as the relative displacements within the textile. Such a distance modification could be caused by the growth or presence of tissue. This distance was measured in both explanted and control prostheses. Ten mesh overlaps, or knots, were randomly chosen in four datasets, two in pristine devices and many more in explants, all segmented as explained in A21. Both Avizo 3D software (different modules) and the Empa Bundle of ImageJ Plugins for Image Analysis (EBIPIA) including the “Canny Edge”, were applied at each segmented knot.

The segment tomogram was first imported into Avizo. Using its “Extract Subvolume” module, an area containing a stitch was selected. A grey image where the voxels belonging to the air surrounding the mesh were first assigned the value of the shortest distance to the nearest branch to be computed. This was done by applying the Boolean “NOT” operator module, followed by the “Distance Map” one. The Euclidean distance map of the (Boolean) “negative” of the stitch was subsequently computed. Such map was a 3D image where each voxel of the air surrounding the knot was assigned a value equal to the distance between the voxel itself and the next unit on this featured structure boundaries.

The second step of the analysis was aimed at measuring characteristic distances between the two mesh branches composing the stitch. T_i was used as the starting point to Euclidean distance map image. The sole voxel values on the ridges of the image itself were selected and their average was computed as the final estimate of the distance between the two branches the stitches. The Euclidean distance map of the surrounding air could be thought of as a landscape in a 4D space; for each point in space surrounding a stitch a topographical height was assigned. The raised part of such 4D landscape was defined as the geometrical *locus* where the height was locally maximised, but also as the *set of all points*, on the two sides of the ridge and along the direction orthogonal to a tangential line from it, where the height decreased rather symmetrically. The features of such points in space are similar to the two sides of the ridge on a mountain top, where the height tends to decrease away from the raised part itself. The ridge of such landscape had the geometrical property of mirroring the curved mesh boundaries. On the ridge of the Euclidean distance map derived from the 3D image, its voxel values represented distances which were identical on both of its sides, thus their duplicates provided a unique definition of the separation between the knot two branches boundary surface. The ridge in a multi-dimensional landscape (mage) is a type of edge, where the gradient of its height acquires impulsively a very large (in theory infinite) value. Therefore to obtain such ridge information, the 3D Euclidean distance map representation of the first step was exported as a stack of 2D images and imported into Fiji. The “Canny Edge” plugin was then applied to it to detect its edges, as explained by Canny. The result was another grey value 3D image where the highest voxel values at edge positions. An isosurface containing a continuous collection of local maxima was then produced, thus locating the ridges between the two branches of the knot. Once such isosurface was identified, its voxels were assigned value equal to one while all the others to zero, in order to create a 3D binary mask mapping out where the ridge was located (A7).

In the end, such mask for the raised part was multiplied by the original Euclidean distance map to produce a final image where only the ridge voxels have non-zero values, which cor-

responded to half of the separation between the two meshes comprising the stitch. Using an in-house developed MATLAB script, the data was extracted and the mean value and standard deviation of the non-zero voxels were computed and multiplied by two, in order to obtain the average distance between the two mesh branches at the knot region.

This procedure to determine the distance of the loops could not be successfully applied to the centre lines alone, the ones previously computed the “Cylinder Correlation” and “Trace Correlation Lines” modules in Avizo 3D. An attempt was made to calculate the distances using the same methodology as describes above, with the difference that, instead of the label image of the meshes, one of the centre lines of those would be used. This would measure the distance between the centres of the meshes, instead of the separation between their edges. The centre lines were computed in Avizo and were stored as a “spatial graph”, a special software data format, which required converting such 3D dataset into a 3D image in TIFF format with the use of the “Convert geometry to label” module (A8-A11).

References

- A1. Schindelin J, Arganda-Carreras I, Frise K, Kayrig V, Longair M, et al. Fiji: an open-source platform for biological-image analysis. *Nat. Methods* 2012; 9: 672-682.
- A2. Buades A, Coll B, Morel JM. A non-local algorithm for image denoising. *IEEE Computer Society Conference on Computer Vision and Pattern Recognition (CUPR'05)*. *Proceed. IEEE Conf. San-Diego USA*. 2005; 60-65.
- A3. Lore C. USG announces the release of Aviso Fire 7, 3D visualization and analysis of software for industrial inspection and materials research. www.ndt.net/search/docs.php3?id=11516&content=1. (Consulted on April 6, 2018).
- A4. Roseman Am. Particle finding in electron micrographs using a fast local correlation algorithm. *Ultramicroscopy*. 2003; 94: 225-236.
- A5. Weber B, Greenan G, Prohaska S, Baum D, Hege HC, et al. Automated tracing of microtubules in electron tomograms of plastic embedded samples of caenorhabditis elegans embryos. *J Struct Biol*. 2012; 178: 129-138.
- A6. Cengiz IF, Oliveira JM, Reis RL. MicroCT a digital 3D microstructural coverage into scaffolds: a systematic review of the reported methods and result. *Biomat Res*. 2018; 22: 26.
- A7. Canny J. A computational approach to edge detection *IEEE Transactions on Patterns Analysis and Machine Intelligence*. PAMI. 1986; 8: 679-698.
- A8. Fisher R, Schlepütz CM, Rossi RM, Derome D, Carmeliet J. Wickling through complex interfaces at interlying yarns. *J Coll Interf Sci*. 2022; 626: 416-425.
- A9. Desplentere F, Lomov SV, Woerdeman DL, Verpoest I, Wevers M, Bogdanovich A. Micro-CT characterization of variability in 3D textile architecture. *Comp. Sci. Technol*. 2005; 65: 1920-1930.
- A10. Garcea SC, Wang Y, Withers PJ. X-ray computed tomography of polymer composites. *Comp Sci Technol*. 2018; 156: 305-319.
- A11. Elliott JC, Dover SD. X-ray microtomography. *J. Microsc*. 1982; 126: 211-213.